

Heterogeneous multiscale Monte Carlo simulations for gold nanoparticle radiosensitization

Martin P. Martinov^{a)} and Rowan M. Thomson^{b)}

email: a) martinov@physics.carleton.ca and b) rthomson@physics.carleton.ca

Carleton Laboratory for Radiotherapy Physics, Department of Physics, Carleton University,
Ottawa, Ontario, K1S 5B6, Canada

Published in Medical Physics Volume 44, Issue 2 in February 2017 (DOI:10.1002/mp.12061)

Abstract

Purpose: To introduce the heterogeneous multiscale (HetMS) model for Monte Carlo simulations of gold nanoparticle dose-enhanced radiation therapy (GNPT), a model characterized by its varying levels of detail on different length scales within a single phantom; to apply the HetMS model in two different scenarios relevant for GNPT and to compare computed results with others published.

Methods: The HetMS model is implemented using an extended version of the EGSnrc user-code `egs_chamber`; the extended code is tested and verified via comparisons with recently-published data from independent GNP simulations. Two distinct scenarios for the HetMS model are then considered: (1) monoenergetic photon beams (20 keV to 1 MeV) incident on a cylinder (1 cm radius, 3 cm length); (2) isotropic point source (brachytherapy source spectra) at the center of a 2.5 cm radius sphere with gold nanoparticles (GNPs) diffusing outwards from the center. Dose enhancement factors (DEFs) are compared for different source energies, depths in phantom, gold concentrations, GNP sizes, and modeling assumptions, as well as with independently published values. Simulation efficiencies are investigated.

Results: The HetMS MC simulations account for the competing effects of photon fluence perturbation (due to gold in the scatter media) coupled with enhanced local energy deposition (due to modeling discrete GNPs within subvolumes). DEFs are most sensitive to these effects for the lower source energies, varying with distance from the source; DEFs below unity (*i.e.*, dose decreases, not enhancements) can occur at energies relevant for brachytherapy. For example, in the cylinder scenario, the 20 keV photon source has a DEF of 3.1 near the phantom's surface, decreasing to less than unity by 0.7 cm depth (for 20 mg/g). Compared to discrete modeling of GNPs throughout the gold-containing (treatment) volume, efficiencies are enhanced by up to a factor of 122 with the HetMS approach. For the spherical phantom, DEFs vary with time for diffusion, radionuclide, and radius; DEFs differ considerably from those computed using a widely-applied analytic approach.

Conclusions: By combining geometric models of varying complexity on different length scales within a single simulation, the HetMS model can effectively account for both macroscopic and microscopic effects which must both be considered for accurate computation of energy deposition and DEFs for GNPT. Efficiency gains with the HetMS approach enable diverse calculations which would otherwise be prohibitively long. The HetMS model may be extended to diverse scenarios relevant for GNPT, providing further avenues for research and development.

1. Introduction

The pioneering work of Hainfield *et al* using gold nanoparticles (GNPs) during irradiation of tumor-bearing mice to increase survival¹ has sparked a large number of studies investigating the potential of GNPs in human radiotherapy treatments. While experimental work investigates various metrics related to the development of GNP dose-enhanced radiation therapy (GNPT), numerical methods are employed to investigate radiation transport and energy deposition due to the limitations of experimental dosimetry in this context. Diverse computational models are employed to study increased energy deposition due to gold nanoparticles, from analytic techniques²⁻⁴ to Monte Carlo (MC) simulations.⁵⁻⁷ In particular, computations are often used to determine the relative increase in dose due to the presence of GNPs, defined as the dose enhancement factor (DEF), *i.e.*, the ratio of dose with GNPs present to that without.

Accurate computations of DEFs in GNPT can present considerable challenges. For realistic radiation therapy scenarios, energy deposition within both the treatment volume and surrounding normal healthy tissues must be considered, resulting in volumes of interest greater than $(1 \text{ cm})^3$. For a frequently-cited concentration of gold (7 mg of gold per g of tissue or water), there may be up to $\sim 10^{16}$ GNPs in $(1 \text{ cm})^3$ of tissue, depending on GNP size. Modeling such a large number of GNPs strains most computational approaches. Within the context of MC simulations, most studies considering whole tumor volumes of interest (millimetres or greater) use a macroscopic model in which voxels represent a homogeneous mixture of soft tissue and gold with a single mass density^{8,9} to avoid modeling large numbers of GNPs. However, this approach may overestimate the effect of GNPs as it does not account for absorption of energy within GNPs themselves and it is the enhanced dose to tissue (not gold) which is the quantity of interest for GNPT. On the other hand, researchers have employed detailed simulations of discrete (not averaged or homogenized) GNPs within tissue/water considering microscopic volumes of interest.^{5,10-12}

Research to connect the macroscopic and microscopic approaches has been limited and varying. To avoid modeling GNPs individually in a macroscopic volume yet still extract the DEF in pure tissue, Koger and Kirkby recently presented a database of factors to convert dose scored in a homogeneous blend of tissue and gold to dose scored in tissue containing discretely-modeled GNPs.¹³ Some researchers have discretely modeled GNPs in a macro-

scopic volume using the simple geometry of a cubic lattice of GNPs embedded in an otherwise homogeneous water or tissue phantom.^{14–18} Cai *et al*¹⁹ used a lattice on a cellular scale, creating a multi-cell configuration containing discretely-modeled GNPs spanning (0.24 cm)³. Douglass *et al*⁶ modeled single shapes (spheres or spherical shells) to represent aggregates of GNPs within a multi-cell model of total volume (0.04 cm)³. While the volumes considered in the latter two studies are above the microscopic scale, they are at least an order of magnitude too small for full GNPT simulations.

The current work focuses on bridging the gap between the microscopic and macroscopic paradigms. We introduce the heterogeneous multiscale (HetMS) model for MC simulations within the context of GNPT, a general framework based on the idea of combining distinct models of varying level of detail on different length scales in a single simulation. In the current work, HetMS models involve homogenized tissue-gold mixtures or pure tissue in larger (\sim cm) volumes and discrete modeling of GNPs embedded in tissue within distinct subvolumes. The HetMS approach is initially presented via example calculations with a cylindrical phantom, in which DEFs are computed at varying depths for photon sources of different energies. A more sophisticated radiotherapy scenario recently presented²⁰ is then considered, determining DEFs and comparing to published values computed with an analytic approach² used in many other studies. Validation of simulations and considerations for future research are discussed.

II. Methods

MC simulations are carried out using the EGSnrc²¹ distribution with the egspc class library.²² The user-code egs_chamber²³ is used due to its variance reduction techniques, but is modified to enable energy-deposition scoring in multiple regions. Transport parameters are generally EGSnrc defaults with the following exceptions: pair angular sampling is turned off, Rayleigh scattering and electron impact ionization are turned on, NRC cross section data are used for bremsstrahlung events and XCOM cross section data²⁴ are used for photon interactions. Explicit M - and N -shell transitions are modeled to account for the dosimetric effects of these atomic relaxations²⁵ (EGSnrc default is to treat M - and N -shell transitions in an average way); note that K - and L -shells are considered explicitly by default. Photons and electrons are simulated down to 1 keV kinetic energy. The high resolution random number generator

option is enabled.

A cubic lattice geometry class is created to efficiently model GNPs within a medium discretely. While cubic lattices have been employed in other studies,^{14,17} the following describes our implementation within EGSnrc for the current work. The cubic lattice class takes a previously-defined geometry, chosen to be a gold sphere in the current work, and places it at (an_x, an_y, an_z) for integers n_x, n_y, n_z and an arbitrary spacing a (which determines gold sphere number density); the same instance of the chosen geometry is placed at all possible positions within a volume. This lattice geometry allows for large reductions in memory used, as well as reducing radiation transport times compared to a simulation in which each GNP geometry is modeled individually. In simulations where the cubic lattice is irradiated by a parallel beam, the lattice is tilted (15° about one perpendicular axis and 30° about the other) relative to the beam axis to avoid shadowing (*i.e.*, having all primary photon trajectories either intersecting with all the GNPs in a row or none at all) which would create a bias that would not exist in a random distribution. Results in this study are not sensitive to the angles chosen as long as the cubic lattice axes are not close to parallel (within 3°) with the beam.

II.A. Verification of MC simulations with GNPs

We perform a verification of our MC simulations involving GNPs using the recent (independent) results of Koger and Kirkby.¹³ Using PENELOPE, these researchers modeled monoenergetic photons or electrons incident on microcavities filled with either randomly-distributed GNPs embedded in ICRU tissue²⁶ or a homogeneous mixture of gold and tissue. Photons and electrons were simulated down to 100 eV, and electrons leaving the microcavity were transported back into it for full energy deposition. Ratios of the dose-to-tissue relative to dose to the homogeneous blend of tissue and gold were published (to allow conversion of dose scored in a mixture to dose-to-tissue) for a range of source energies and GNP concentrations.¹³

In the current work, dose ratios (dose-to-tissue relative to dose-to-mixture of tissue and gold) are calculated with simulations involving cylindrical geometries. A monoenergetic (20, 30 or 50 keV) parallel photon beam (circular cross section, 150 μm radius) is incident on a cylinder (150 μm radius, 200 μm long) containing either a lattice of GNPs (20 or 100 nm

diameter) embedded in pure ICRU tissue²⁶ or a homogeneous mixture of gold and ICRU tissue (concentrations of 5, 10 and 20 mg/g). Dose is scored in a smaller cylinder (100 μm radius, 100 μm long) located at the center of the larger cylinder (see Fig. 1). The dose ratio (or conversion factor) is computed by taking the ratio of the doses scored in the GNP lattice to homogeneous scenarios.

Fig 1

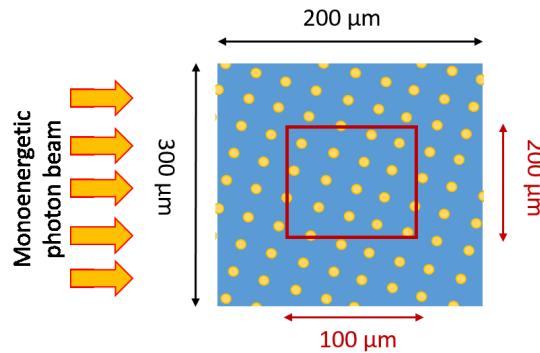


Figure 1: Schematic diagram for verification of MC simulations with GNPs: cross section of the cylindrical phantom comprised of a lattice of GNPs embedded in tissue; the scoring region, outlined in red, is at the center of the larger phantom. For the homogeneous scenario, the cylindrical phantom consists of a single medium that is a homogeneous mixture of gold and tissue.

II.B. Parallel beam of monoenergetic photons incident on cylinder

For the first set of calculations using the HetMS model, parallel beams (circular cross section, 1 cm radius) of monoenergetic photons with energies 20, 30, 50, 90, and 200 keV, as well as 1 MeV are incident on cylindrical phantoms (1 cm radius, 3 cm long), depicted in Fig. 2. In the HetMS model, the cylinder is comprised of a homogeneous mixture of ICRU tissue²⁶ and gold, containing smaller cylinders (100 μm radius, 100 μm long) comprised of a lattice of discretely-modeled spherical GNPs within (pure) ICRU tissue (Fig. 2a). A total of 119 smaller cylinders evenly-spaced along the central axis of the cylindrical phantom are simultaneously modeled and energy deposited within the tissue (not GNPs) is scored. For comparison, a fully homogeneous cylinder is modeled in which all regions are a mixture of tissue and gold and dose is scored therein (Fig. 2b). Simulations are then repeated with a tissue-only phantom to provide the denominators for computation of DEFs (Fig. 2c). Simulations are performed for concentrations of 5, 10 and 20 mg/g, and GNP diameters of 20 and 100 nm. Results for the HetMS model (Fig. 2a) are compared to those from simula-

Fig 2

tion of the cylinder comprised of tissue entirely filled with a GNP lattice (for a subset of source energies and gold concentrations) for further validation, as well as characterization of simulation efficiencies.

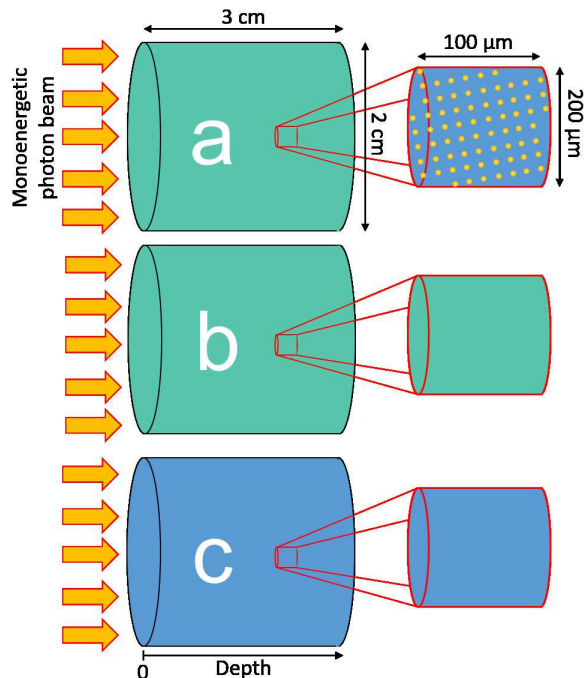


Figure 2: Schematic diagrams for cylindrical phantom simulations: (a) HetMS model with homogeneous gold-tissue phantom with 119 smaller cylinders consisting of GNPs embedded in tissue placed at even intervals along the central axis; (b) corresponding fully homogeneous (gold-tissue mixture) phantom; and (c) pure tissue phantom.

II.C. Brachytherapy source in a sphere with varying gold concentration

The second scenario modeled in the HetMS framework is from the work of Sinha *et al*²⁰ who considered a polymer film embedded with GNPs coated on the inter-seed spacers used in prostate permanent implant brachytherapy; the film dissolves over time in the patient, releasing GNPs which diffuse outward to create a significant concentration of gold in the treatment volume. Sinha *et al* calculated DEFs using a previously-developed analytical calculation approach:² calculations were performed at different radii within a water sphere containing an isotropic point source (¹²⁵I, ¹⁰³Pd and ¹³¹Cs) at its center. Assuming GNPs steadily released from the sphere center and, using Fick's second law of diffusion,²⁷ GNP concentration was determined as a function of time and radial position within the sphere,

enabling computation of DEFs. No particular localization of GNPs within tumor cells was assumed, *i.e.*, GNPs randomly arranged within a region of a given concentration.

In the HetMS model simulation of the above scenario, a 2.5 cm radius sphere divided into 0.5 mm shells each containing a homogeneous mixture of gold and water with concentrations based on the diffusion of GNPs from the center is modeled (Fig. 3). The 50 shells are a discrete approximation of the continuous decrease in concentration expected. At the center of each homogeneous shell, a 100 μm thick spherical shell comprised of 20 nm diameter GNPs in a lattice embedded in water is modeled, and dose is scored in water within these regions. An isotropic point source at the center of the sphere is used assuming the spectra leaving the following seed models:²⁸ OncoSeed 6711^{29,30} (¹²⁵I), IsoRay CS1^{31,32} (¹³¹Cs), and TheraSeed 200^{32,33} (¹⁰³Pd). Simulations are repeated with an all-water geometry (no gold) to provide the denominators to compute DEFs.

Fig 3

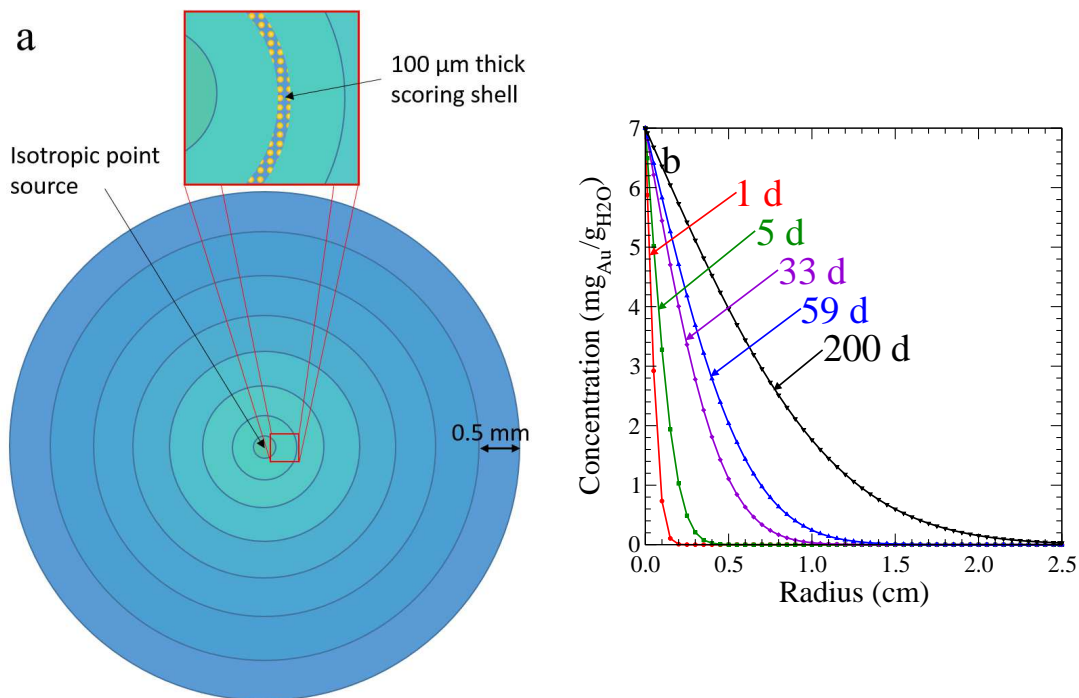


Figure 3: (a) Schematic cross-sectional diagram of the sphere with GNPs released from its center; homogeneous water-gold mixtures are modeled in spherical shells 0.5 mm thick. A 100 μm thick spherical shell consisting of discretely-modeled GNPs in water (shown above) is embedded in each shell. (b) Gold concentrations within the sphere as a function of radius for different times after implantation assuming 7 mg Au/g water at the center and following Fick's second law of diffusion.

III. Results

III.A. Verification of MC simulations with GNPs

Table 1 presents dose ratios (dose-to-tissue relative to dose to a homogeneous tissue-gold mixture) for various gold concentrations and source energies. While many values computed in the current work agree with the published values of Koger and Kirkby¹³ within the 1σ statistical uncertainties indicated, all values agree within 2σ uncertainties except for the 20 keV beam with 20 nm diameter GNPs at a concentration of 20 mg/g, which is at 2.1σ . The largest percent difference observed is 2.6% for the 50 keV beam with 20 nm diameter GNPs having a concentration of 20 mg/g (quadrature sum of the 1σ statistical uncertainties is 1.3%). The absolute difference between our results and those of Koger and Kirkby averaged over all the source energies, GNP diameters, and gold concentrations considered is 0.92%. Simulations repeated with larger cylindrical phantoms (radii of 200 or 300 μm rather than 150 μm , lengths of 300 or 400 μm rather than 200 μm) but with the same central scoring volume (radius 100 μm , length 100 μm) yield dose ratios in agreement within statistical uncertainties.

Table 1: Verification of Monte Carlo simulations: Comparison of dose ratios (dose-to-tissue relative to dose to a homogeneous tissue-gold mixture) for 20 and 100 nm diameter GNPs for the current work (Fig. 1) and the independent results of Koger and Kirkby.¹³ Statistical uncertainty (1σ) on the final digit(s) is indicated in parentheses.

GNP		20 nm diam. GNPs		100 nm diam. GNPs	
Concentration ($\text{mg}_{\text{Au}}/\text{g}_{\text{tissue}}$)	Energy (keV)	Koger and Kirkby	This work	Koger and Kirkby	This work
5	20	0.949 (6)	0.951 (3)	0.884 (7)	0.882 (3)
	30	0.969 (8)	0.963 (5)	0.927 (7)	0.930 (5)
	50	0.984 (12)	0.990 (9)	0.974 (10)	0.950 (9)
10	20	0.937 (6)	0.926 (2)	0.827 (6)	0.824 (2)
	30	0.950 (8)	0.947 (4)	0.910 (7)	0.901 (4)
	50	0.984 (11)	0.968 (8)	0.946 (10)	0.952 (7)
20	20	0.917 (7)	0.902 (2)	0.791 (6)	0.782 (2)
	30	0.952 (8)	0.939 (3)	0.881 (7)	0.875 (3)
	50	0.986 (11)	0.961 (6)	0.942 (10)	0.929 (6)

III.B. Parallel beam of monoenergetic photons incident on cylinder

The results of the cylinder simulations for 20 nm diameter GNPs are summarized in Figure 4. Focusing first on photon source energies below 200 keV, DEFs for all concentrations are most substantial near the surface of the phantom, ranging from 1.6 to 4.2, and decrease with depth. DEFs decrease more rapidly with increasing depth in the 20 mg/g case: for the 50 keV source, DEFs decrease from 4 to 2.5 over the 3 cm length of the phantom, while DEFs for the 20 keV source are near 3 at the surface and decrease nearly to zero. DEFs decrease below unity for some gold concentrations and source energies: for 5 mg/g and a 20 keV source, there are DEFs < 1 for depths of 1 cm or more; for 10 and 20 mg/g, DEFs drop below unity within the 3 cm long phantom for a 30 keV beam as well. These phenomena arise due to competing effects of enhanced local energy deposition (due to photoelectric interactions in local GNP) and decreasing fluence with depth (due to the presence of gold between the front of the cylinder and the scoring depth, *i.e.*, within the scatter media), and are expected on the basis of energy conservation. When the effects of the decreasing fluence exceed local energy deposition gains, dose scored within the HetMS model is lower than that in the pure tissue phantom (no gold), resulting in DEFs below unity, *i.e.*, dose *decreases* not *enhancements*, making DEF a misnomer. Despite this, the dose ratio will continue to be referred to as a DEF for the purposes of continuity.

Fig 4

As source energy increases, the relative importance of photoelectric events decreases resulting in DEFs nearer unity and less variation in DEFs with depth. For 200 keV photons, DEFs are approximately constant with depth within the 3 cm phantom, at a value near 1.05 for 5 mg/g and 1.40 for 20 mg/g. For the 1 MeV beam, incoherent (Compton) interactions dominate resulting in DEFs near unity for the length of the cylinder – no significant dose enhancement.

DEFs computed with 20 or 100 nm diameter GNPs in scoring regions (HetMS model) along with the homogenized tissue-gold mixture are summarized in Figure 5 for the 20 keV photon source. In general, DEFs within the homogeneous model (qualitatively) follow the same trends as those in the HetMS model, showing competition between attenuation of fluence and enhanced energy deposition. However, for all gold concentrations and GNP diameters, DEFs computed within the homogeneous model overestimate those for the HetMS model: discrepancies are as large as 20% for the 20 keV beam and vary with depth. As source

Fig 5

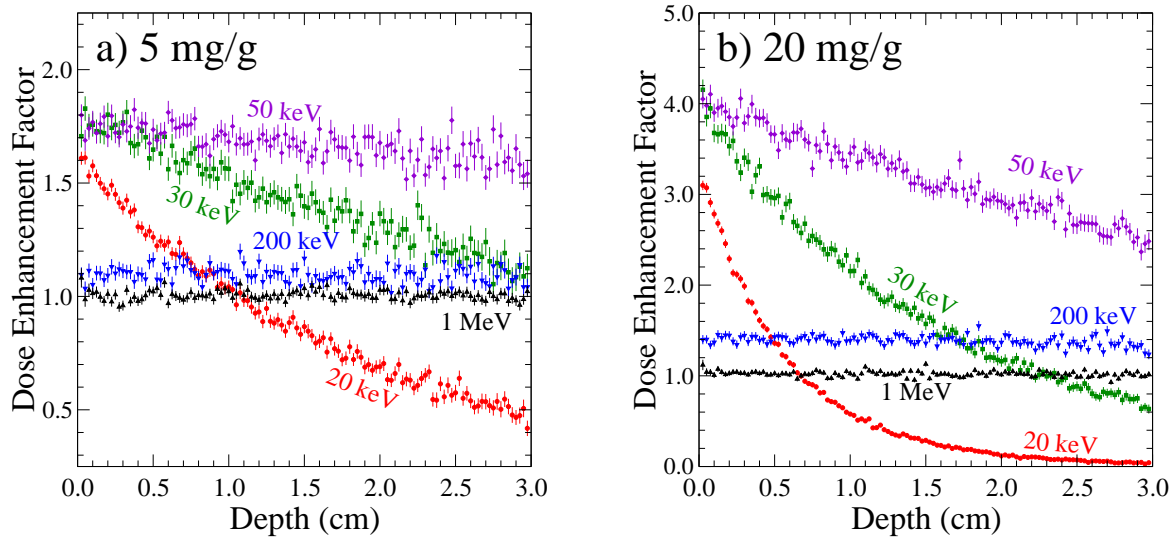


Figure 4: DEFs versus depth within the cylindrical phantom (Fig. 2) with concentrations of (a) 5 and (b) 20 mg of Au per g of tissue for 20 nm diameter GNPs with incident photon source energies of 20 keV to 1 MeV. DEFs for 90 keV which show smaller magnitude but similar trends to the results for 50 keV are omitted for clarity. Results for simulations with a concentration of 10 mg/g (omitted) exhibit similar trends to 5 and 20 mg/g.

energy increases, discrepancies between DEFs computed with the HetMS and homogenized models decrease (results not shown; see also dose ratios presented in table 1, section III.A.). The overestimation observed for DEFs computed in the homogenized model stems from the inclusion of energy deposited within gold into the total ‘enhanced’ dose, while it is only dose to tissue (not gold) that is relevant for GNPT.^{10,15} In the HetMS simulations with GNPs modeled discretely and dose in tissue scored, photoelectrons generated in the gold may deposit all their energy in the gold or they must travel some distance (and deposit energy) before entering tissue. By energy conservation, there is then less dose in the numerator for the computation of DEFs. Comparing HetMS model results for 20 and 100 nm diameter GNPs but same total gold concentration, DEFs are consistently higher with smaller GNPs for lower source energies (20 and 30 keV) but do not vary significantly at higher energies. Sensitivity to GNP size stems from the re-absorption of electrons generated within GNPs which is more important for larger GNPs.^{10,15}

All results presented with the HetMS model thus far might have been carried out in a phantom with each GNP modeled discretely, rather than combining models with different features on different keV length scales, as done for the HetMS model. We carried out a subset

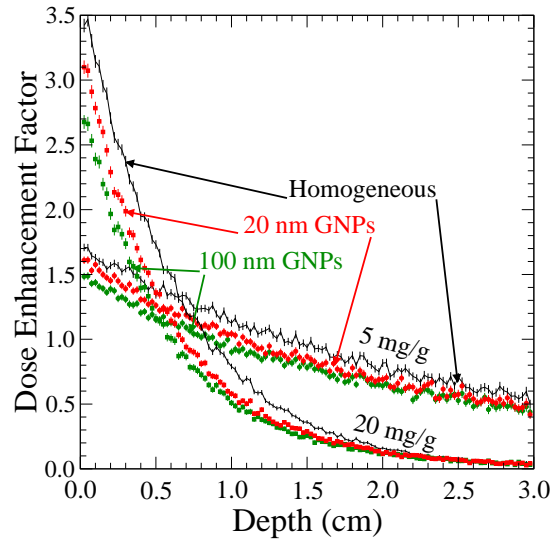


Figure 5: DEFs versus depth within the cylindrical phantom (Fig. 2) with concentrations of 5 and 20 mg/g for 20 and 100 nm diameter GNPs with 20 keV incident photons. DEFs computed for the 30 and 50 keV source energies show similar trends to the 20 keV case but are omitted for clarity.

of simulations in a cylindrical phantom comprised of ICRU tissue with a lattice of GNPs spanning the entire phantom, and results agreed with those computed within the HetMS model with GNPs only modeled in subvolumes (Fig. 2) within statistical uncertainties. The major difference between the two sets of simulations was time or, equivalently, efficiency:

$$\epsilon = \frac{1}{s^2 t}, \quad (1)$$

where t is the simulation time and s is the average percent uncertainty on doses in the 119 scoring regions (spanning the 3 cm long cylindrical phantom). Table 2 demonstrates considerable efficiency gains with the HetMS model compared with having a lattice filling the entire volume of interest, with efficiencies enhanced by factors of 24 (20 mg/g; 20 keV) to 122 (5 mg/g; 50 keV); HetMS simulations have lower efficiencies than the corresponding (inaccurate) homogeneous models by 15% (5 mg/g; 20 keV) to 31% (20 mg/g; 20 keV). Efficiencies vary with source energy and gold concentration, *e.g.*, the lower efficiency of the 20 keV photons and gold concentration 20 mg/g reflects larger statistical uncertainties at depth in the cylinder (due to considerable attenuation of these relatively low energy photons with the higher concentration of gold).

Simulation times (on a single Intel Xeon 5160 core) may be deduced from the results

in Table 2: for the concentrations and source energies considered therein, HetMS simulation times for $s = 2\%$ average uncertainty range from 0.12 years (5 mg/g; 50 keV) to 0.91 years (20 mg/g; 20 keV) while full lattice simulation times range from 3.9 years (5 mg/g; 20 keV) to 22 years (20 mg/g; 20 keV). The results presented in Figs. 4 and 5 are from simulations of $> 10^{10}$ histories, with number of histories adjusted to achieve the relatively small error bars (depending on source energy and gold concentration). We have not included the times for these particular calculations because simulations were run on multi-core clusters with CPUs of varying speeds, and hence these calculation times (or efficiencies) are not representative measures.

Table 2: Example efficiencies (Eq. 1) for HetMS simulations in the cylindrical phantom (Fig. 2a), with efficiencies relative to the tissue cylinder entirely filled with a lattice (“HetMS/Lattice”) and to the homogeneous gold-tissue mixture cylinder (Fig. 2b; “HetMS/Homog”). Estimates of efficiencies are based on calculation times for simulation of 3.6×10^6 histories on a single thread Intel Xeon 5160 (3.00 GHz) core. The time to achieve $s = 1\%$ is $1/\epsilon$.

Concentration (mg _{Au} /g _{tissue})	Energy (keV)	Efficiency HetMS (h ⁻¹)	Relative efficiency	
			HetMS/Lattice	HetMS/Homog
5	20	2.2×10^{-4}	29	0.85
	50	2.4×10^{-4}	122	0.69
20	20	3.1×10^{-5}	24	0.73
	50	2.1×10^{-4}	89	0.72

III.C. Brachytherapy source in a sphere with varying gold concentration

DEFs as a function of radius computed within the HetMS model for the spherical phantom with varying gold concentration (Fig. 3) are shown in Fig. 6a for ¹²⁵I at different times. Near the source, the DEFs range from 1.4 after 1 day to near 1.9 after 33 days or more. DEFs go to unity at small radii for the 1 and 5 day cases, whereas decreases in DEFs to unity happen at larger radii later in the treatment (33 days or more). For each treatment time considered, DEFs drop below one at some radius, *e.g.*, 0.35 cm for 5 days, 0.7 cm for 33 days, and 1.2 cm for 200 days. As observed in the cylindrical phantom computations (section III.B.), DEFs < 1 correspond to a dose decrease due to decreasing fluence resulting from gold between the source and scoring regions. For the current spherical geometry involving varying gold

Fig 6

concentrations (Fig. 3b), dose decreases are observed in regions where there is a non-zero concentration of gold, as well as at larger radii where effectively no GNPs have diffused. Similar trends are observed for the ^{131}Cs and ^{103}Pd sources (Fig. 6b), however, exact DEF values depend on radionuclide source spectrum, with lower (higher) DEFs for ^{103}Pd (^{131}Cs) compared to ^{125}I .

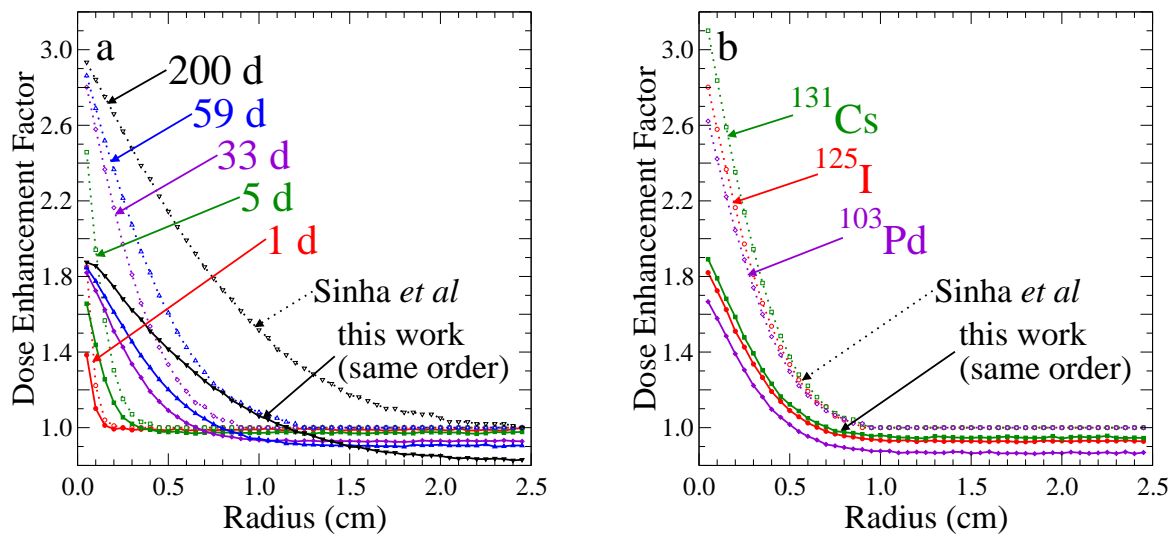


Figure 6: (a) DEF versus radius within the spherical phantom (Fig. 3) at different times during treatment with ^{125}I . (b) Comparison of DEF versus radius for different radionuclides after 33 days. Both panels present results of the current work (closed symbols and solid lines; error bars for statistical uncertainties are often too small to see) as well as data extracted from Sinha *et al.*²⁰ using plot digitization (open symbols and dotted lines).

DEFs from Sinha *et al.*²⁰ are presented alongside the HetMS results in Fig. 6. While both sets of DEFs follow the same trends, they differ considerably: DEFs computed by Sinha *et al.* are consistently higher for all radii and times, and for all three radionuclides. For early times in the treatment (1 and 5 days), 40% discrepancies are observed near the source, but agreement is better near a radius of 5 mm where little gold has diffused. For later times (33 days or more), differences range from 5 to 50%. Most notably, DEFs computed by Sinha *et al.* never drop below one – all DEFs converge to unity with increasing radius whereas the effects of increased fluence perturbation with radius (due to gold), seen in HetMS results in Fig. 6, are not apparent.

IV. Discussion

The cylindrical and spherical phantom examples illustrate the main ideas of the HetMS model for GNPT: distinct models are employed on different length scales in order to capture relevant physics effects within a single, relatively efficient, simulation. While these ideas are generalizable to consider many issues in GNPT using the HetMS approach (more below), the current work focuses on relatively simple HetMS models involving homogenized tissue-gold mixtures (or pure tissue) in the bulk of phantoms (possibly with varying gold concentration) with 50 or 119 microscopic regions containing discretely-modeled GNPs in tissue. Employing the homogenized, tissue-gold mixture (or pure tissue) within the bulk of the phantom enables realistic representation of scatter conditions and determination of fluence. The discrete modeling of GNPs within smaller ($\sim\mu\text{m}$) regions enables scoring of energy deposition within the tissue in which GNPs are embedded.

The lattices employed herein for modeling arrays of GNPs are not *required* as part of the HetMS approach, rather, they may be a useful approach for geometry specification. Lattices have been employed elsewhere for GNPT (discussed above; Refs.^{14–19}), but they have not been combined with the homogenized tissue-gold mixtures as done within our HetMS models, nor used within more sophisticated phantoms with multiple GNP lattices to model varying gold concentrations (spherical phantom simulations, section III.C.). Furthermore, the HetMS approach enables considerably more efficient simulations than otherwise possible with discrete modeling of GNPs throughout the entire GNP-containing volume (as done previously^{14–19}). We observed efficiency gains of factors of up to 122 within the cylindrical phantom (table 2), with efficiency gains varying with source energy and gold concentration. In general, efficiency gains would depend on the details of the geometry considered, *e.g.*, phantom size; number, size, and geometries of scoring regions; GNP concentration, source energy, and so on. In certain circumstances, discrete modelling of each GNP within the macroscopic volume would be impossible with available computer resources (memory, computing time). Indeed, calculation times for the simulations presented herein would have been prohibitively long without the HetMS approach – performing the current study using discrete modeling of every GNP within the phantoms would have been computationally infeasible. *All* of the cylindrical phantom simulations were completed in less time than it would take to run the cylindrical simulation modeling discrete GNPs everywhere for *only* an energy of

20 keV and concentration of 20 mg/g.

DEFs computed for the cylindrical phantom scenario (section III.B.) demonstrate the competing effects of enhanced local energy deposition and decreasing fluence with depth in the phantom. While dose enhancements are observed for many source energies, DEFs change considerably with depth: DEFs < 1 are observed for lower energy sources (20, 30 keV) within the phantom. These dose decreases have the potential to create cold spots in a treatment volume and must be accounted for in any algorithm for GNPT dosimetry or treatment planning.

The results of our cylinder simulations are generally comparable with those presented in other published works. For example, the magnitudes of DEFs observed at the front of the cylindrical phantom for 20 and 30 keV sources (Fig. 4) are generally in agreement with those predicted by Roeske *et al* for ^{103}Pd and ^{125}I using analytic calculations.³⁴ Results of some other works show gradients in DEFs over $\sim\text{cm}$ length scales (although often not dose decreases, DEFs < 1), *e.g.*, MC models employing a $(1\text{ cm})^3$ lattice of GNPs and considering kilovoltage photon/brachytherapy sources,^{15,17} as well as MC models involving homogenized tissue-gold mixtures (no discrete modelling of GNPs) irradiated by ^{125}I , 50 kVp x ray, and ^{169}Yb sources.⁹ In contrast, results of the similar work of Mesbahi *et al* (who modeled a $(1\text{ cm})^3$ region containing a lattice of GNPs (of varying diameter; concentrations of 7 and 18 mg/g) within a larger phantom) do not have a downward trend in DEFs with depth. This is likely due to the relatively low resolution of their dose scoring grid, the shorter distance (1 cm) they considered within the region containing GNPs (along with the magnitude of statistical uncertainties), or the fact that the lattice had an axis aligned with the parallel beam incident on the phantom (see Fig. 1 in Mesbahi *et al*¹⁴). Within the context of tumor dose enhancement using modified megavoltage beams and gadolinium or iodine contrast media (not GNPT), Robar *et al* noted decreasing trends in dose enhancement over centimeter length scales.³⁵

With the potential for considerable DEFs at kilovoltage energies, previous studies have investigated DEFs for brachytherapy involving GNPs (see, *e.g.*, Refs.^{5,9-11,15,17}). Recent works considered new avenues for GNP delivery within the context of accelerated partial breast irradiation with an electronic brachytherapy source³⁶ and prostate brachytherapy²⁰ with GNPs diffusing within the treatment volume. Our spherical phantom simulations con-

sidered the latter scenario, with considerable discrepancies (up to 50%) observed between the published DEFs computed by Sinha *et al* and those from our HetMS model (Fig. 6).

Sinha *et al* indicate 10% uncertainties on their DEFs,²⁰ citing another work dealing with dose enhancement to endothelial cells via megavoltage x rays and GNPs,³⁷ however, it is unclear where the figure of 10% originates given the different considerations for the kilovoltage sources in the brachytherapy context. Uncertainties of 10% do not account for the observed discrepancies in Fig. 6. While seed models and spectra of Sinha *et al* were unspecified, different spectra do not explain discrepancies as we found relatively small variations in DEFs computed assuming different spectra of the same radionuclide. Sinha *et al* further note that their analytic approach² to compute DEFs has been validated against MC results in previous publications.²⁰ However, there are many approximations in this analytic calculation that are questionable in the current context, *e.g.*, ignoring the effects of scatter and attenuation of primary photons due to gold. These approximations may result in the considerable discrepancies between the DEFs computed via the analytic approach and the HetMS model. The validity of the assumptions of this analytic approach² across the diverse published applications^{3,20,36,37} is doubtful.

Validation of computational models used to determine DEFs is generally challenging due to the lack of experimental data for comparison and difficulties in cross comparisons between distinct published (computational) works with their differences in geometries, modeling assumptions, sources, *etc.* For the current work, with the alterations to `egs_chamber` and the creation of the lattice geometry, the code was tested for self-consistency. Simulations were tested for robustness under variations in transport parameters. The use of 1 keV energy transport cutoffs for photons and electrons was investigated by repeating simulations with these cutoffs increasing in 125 eV increments up to 2 keV (*i.e.*, 1.000 keV, 1.125 keV, 1.250 keV, ..., 2.000 keV); results agreed within statistical uncertainties up to 1.75 keV. Several results in Fig. 4 were replicated using 10 μm long scoring cylinders instead of 100 μm cylinders, hence demonstrating insensitivity to variations in the μm scoring region dimensions.

The demonstrated agreement between our results and those of Koger and Kirkby (Table 1, section III.A.) from their PENELOPE simulations (100 eV transport cutoff) provides validation of our simulations, demonstrating the appropriateness of EGSnrc with its condensed

history (CH) approach (class II scheme³⁸), as well as our 1 keV transport cutoff and lattice geometry, for the scenarios considered herein. Cai *et al* noted good agreement when comparing their MCNP5 (CH algorithm for electrons, 1 keV transport cutoffs) results within μm -scale cell compartments (cell and nucleus diameters of 18.6 μm and 12.6 μm , respectively)¹⁹ to those previously published using PENELOPE¹⁰ (50 eV electron cutoff) when scoring in microscopic regions. These observations support the use of CH codes and ~ 1 keV transport cutoffs in GNPT scenarios in which energy deposition need not be resolved on nm length scales (40 nm range of 1 keV electron in water³⁹) and when self-absorption of sub-1 keV electrons within GNPs^{7,10} is relatively unimportant. While use of such CH codes and 1 keV transport cutoffs enhance simulation efficiency, thus making simulations possible with available computing power, some GNPT applications require consideration of electron transport to lower energies and event-by-event simulation of electron transport (with various associated challenges⁴⁰⁻⁴²). These applications include quantification of energy deposition with $\sim\text{nm}$ resolution in the immediate vicinity of GNPs towards understanding possible considerable DEF variability on nm length scales.^{11,43}

In their recent review article,⁴² Zygmanski and Sajo emphasized the importance of multi-scale considerations for GNPT. The relevant discussion regarding simulation mainly focused on a two-stage approach, *e.g.*, first calculating a phase space within an efficient macroscopic phantom and then creating a microbeam in a more detailed microscopic phantom (see Ref.⁴² and references therein). This approach involves two separate simulations and sometimes different macro/micro codes; typically, only a few depths within a phantom are considered.¹⁰⁻¹² However, as seen in Figs. 4-6, variations in DEFs with depth may be considerable and of importance for prospective clinical GNPT scenarios; indeed, variations in DEFs with depth may be more considerable than much-studied variations of DEFs with source energy or gold concentration (see Ref.⁴² and references therein). In contrast to the two-stage approach, the HetMS concept enables a single relatively-efficient simulation modeling both macro- and microscopic geometries: energy deposition may be computed within multiple microscopic regions throughout the macroscopic phantom while still accounting for scatter conditions.

The HetMS approach described herein may be both implemented and applied in diverse ways for GNPT. While we implemented the HetMS model within EGSnrc, the ideas are not limited to one code system and might be implemented in different codes. Advanced geometry modeling packages/capabilities would be a requirement of such a code; any efficiency gains

would depend on the code details including geometry modeling approach, variance reduction techniques, etc. Code choice would also be influenced by the application considered, *e.g.*, whether simulation of radiation transport to sub-1 keV energies is needed. Such considerations are required in the investigation of interactions of radiation in the vicinity of DNA and GNPs⁴⁴ or quantification of highly localized (nm) dose enhancement in the immediate vicinity of a GNP.^{5,10,11} Radiation transport modeling could be different within distinct parts of the HetMS model, *e.g.*, lower transport cutoffs and distinct transport algorithms within the microscopic geometry. Diverse GNPT scenarios including different possible radiotherapy sources^{34,43} could also be considered with the HetMS approach, computing various quantities of interest beyond tissue cavity DEFs and nuclear DEFs, *e.g.*, spectra of radiation quanta within different regions or emitted from GNPs,¹⁰ enhanced energy deposited within mitochondria.^{12,45}

While our example simulations generally involved two distinct scales (1 – homogeneous gold-tissue mixtures; 2 – discrete GNPs embedded in tissue), there could be more than two ‘levels’ of detail: different models on multiple scales in order to accurately model radiation transport and energy deposition. Larger and more detailed phantoms might be considered. Microscopic regions could have varying and more detailed arrangements of GNPs within cells^{10,46} according to biological distribution (including possible clustering), with subcellular structures included, *e.g.*, nucleus, mitochondria, DNA,^{6,12,45} towards understanding the biological effects of such treatments. These studies, coupled with work on radiobiological effect, might help in exploring unanswered questions within the field of GNPT, *e.g.*, decreased cell survival in GNP treatments in the megavoltage range.^{44,47}

V. Conclusion

The current work presents a simultaneous multiscale approach, described as the heterogeneous multiscale (HetMS) model, accounting for both macroscopic and microscopic considerations in a single simulation to accurately model the effects of GNPs within the radiotherapy context. We have demonstrated the HetMS approach within the simple model of a cylindrical phantom consisting of homogeneous gold-tissue mixture in which microscopic regions of discretely-modeled GNPs in tissue are embedded, as well as within a recently-proposed prostate brachytherapy scenario involving GNPs diffusing from spacers. The HetMS ap-

proach enables consideration of both scatter conditions and changes in fluence over the averaged gold-tissue medium, as well as scoring in tissue containing GNPs but not within the GNPs themselves. Compared to discretely-modeling GNPs throughout the gold-containing volume, efficiency gains of factors of up to 122 were observed with HetMS simulations, enabling the calculations within the diverse scenarios considered herein with available computing power. Both sets of example calculations demonstrate considerable and varying dependence of DEFs with depth in tissue, gold concentration, GNP size, and source energy. These results, as well as observed discrepancies with DEFs computed using a broadly-applied analytic technique involving considerable approximations, emphasize the importance of HetMS modeling for lower source energies, *e.g.*, brachytherapy or orthovoltage treatments using GNPs. The HetMS MC simulations may be extended in various ways, offering new avenues for GNPT research.

Acknowledgements

The authors acknowledge support from the Natural Sciences and Engineering Research Council of Canada (NSERC), Canada Research Chairs (CRC) program, an Early Researcher Award from the Ministry of Research and Innovation of Ontario, and the Carleton University Research Office, as well as access to computing resources from Compute/Calcul Canada and the Shared Hierarchical Academic Research Computing Network (SHARCNET). The authors declare that they do not have any conflict of interest.

References

- ¹ J. F. Hainfeld, D. N. Slatkin, and H. M. Smilowitz, The use of gold nanoparticles to enhance radiotherapy in mice, *Phys. Med. Biol.* **49**, N309–N315 (2004).
- ² W. Ngwa, G. M. Makrigrorios, and R. I. Berbeco, Applying gold nanoparticles as tumor-vascular disrupting agents during brachytherapy: estimation of endothelial dose enhancement, *Phys. Med. Biol.* **55**, 6533 – 6548 (2010).
- ³ W. Ngwa, G. M. Makrigrorgos, and R. I. Berbeco, Gold nanoparticle-aided brachytherapy with vascular dose painting: Estimation of dose enhancement to the tumor endothelial cell nucleus, *Med. Phys.* **39**, 392–398 (2012).

- ⁴ W. Ngwa, G. M. Makrigroros, and R. I. Berbeco, Gold nanoparticle enhancement of stereotactic radiosurgery for neovascular age-related macular degeneration, *Phys. Med. Biol.* **57**, 6371 – 6380 (2012).
- ⁵ B. L. Jones, S. Krishnan, and S. H. Cho, Estimation of microscopic dose enhancement factor around gold nanoparticles by Monte Carlo calculations, *Med. Phys.* **37**, 3809 – 3816 (2010).
- ⁶ M. Douglass, E. Bezak, and S. Penfold, Monte Carlo investigation of the increased radiation deposition due to gold nanoparticles using kilovoltage and megavoltage photons in a 3D randomized cell model, *Med. Phys.* **40**, 071710 (9 pp) (2013).
- ⁷ M. K. Leung, J. C. Chow, B. D. Chithrani, M. J. Lee, B. Oms, and D. A. Jaffray, Irradiation of gold nanoparticles by x-rays: Monte Carlo simulation of dose enhancements and the spatial properties of the secondary electrons production, *Med. Phys.* **38**, 624 – 631 (2011).
- ⁸ S. H. Cho, Estimation of tumour dose enhancement due to gold nanoparticles during typical radiation treatments: a preliminary Monte Carlo study, *Phys. Med. Biol.* **50**, N163 – N173 (2005).
- ⁹ S. H. Cho, B. L. Jones, and S. Krishnan, The dosimetric feasibility of gold nanoparticle-aided radiation therapy (GNRT) via brachytherapy using low-energy gamma-/x-ray sources, *Phys. Med. Biol.* **54**, 4889–4905 (2009).
- ¹⁰ E. Lechtman, N. Chattopadhyay, Z. Cai, S. Mashouf, R. Reilly, and J. P. Pignol, Implications on clinical scenario of gold nanoparticle radiosensitization in regards to photon energy, nanoparticle size, concentration and location, *Phys. Med. Biol.* **56**, 4631 – 4647 (2011).
- ¹¹ P. Zygmanski, B. Liu, P. Tsiamas, F. Cifter, M. Petersheim, J. Hesser, and E. Sajo, Dependence of Monte Carlo microdosimetric computations on the simulation geometry of gold nanoparticles, *Phys. Med. Biol.* **58**, 7961–7977 (2013).
- ¹² C. Kirkby and E. Ghasroddashti, Targeting mitochondria in cancer cells using gold nanoparticle-enhanced radiotherapy: A Monte Carlo study, *Med. Phys.* **42**, 1119 – 1128 (2015).
- ¹³ B. Koger and C. Kirkby, A method for converting dose-to-medium to dose-to-tissue in Monte Carlo studies of gold nanoparticle-enhanced radiotherapy, *Phys. Med. Biol.* **61**, 2014–2024 (2016).
- ¹⁴ A. Mesbahi, F. Jamali, and N. Gharehaghaji, Effect of photon beam energy, gold nanoparticle size and concentration on the dose enhancement in radiation therapy, *Bioimpacts* **3**, 29 (2013).

- 15 M. Ghorbani, D. Pakravan, M. Bakhshabadi, and A. S. Meigooni, Dose enhancement in brachytherapy in the presence of gold nanoparticles: a Monte Carlo study on the size of gold nanoparticles and method of modelling, *Nukleonika* **57**, 401–406 (2012).
- 16 M. Ghorbani, M. Bakhshabadi, A. Golshan, and C. Knaup, Dose enhancement by various nanoparticles in prostate brachytherapy, *Australasian Physical & Engineering Sciences in Medicine* **36**, 431–440 (2013).
- 17 S. X. Zhang, J. Gao, T. A. Buchholz, Z. Wang, M. R. Salehpour, R. A. Drezek, and T.-K. Yu, Quantifying tumor-selective radiation dose enhancements using gold nanoparticles: a monte carlo simulation study, *Biomedical microdevices* **11**, 925–933 (2009).
- 18 M. T. B. Toossi, M. Ghorbani, M. Mehrpouyan, F. Akbari, L. S. Sabet, and A. S. Meigooni, A Monte Carlo study on tissue dose enhancement in brachytherapy: a comparison between gadolinium and gold nanoparticles, *Australasian Physical & Engineering Sciences in Medicine* **35**, 177–185 (2012).
- 19 Z. Cai, J. Pignol, N. Chattopadhyay, Y. L. Kwon, E. Lechtman, and R. M. Reilly, Investigation of the effects of cell model and subcellular location of gold nanoparticles on nuclear dose enhancement factors using Monte Carlo simulation, *Med. Phys.* **40**, 114101 (2013).
- 20 N. Sinha, G. Cifter, E. Sajo, R. Kumar, S. Sridhar, P. L. Nguyen, R. A. Cormack, G. M. Makrigiorgos, and W. Ngwa, Brachytherapy Application With In Situ Dose Painting Administered by Gold Nanoparticle Eluters, *Int. J. Radiat. Oncol. Biol. Phys.* **91**, 385–392 (2015).
- 21 I. Kawrakow, E. Mainegra-Hing, D. W. O. Rogers, F. Tessier, and B. R. B. Walters, The EGSnrc Code System: Monte Carlo simulation of electron and photon transport, NRC Technical Report PIRS-701 v4-2-3-2, National Research Council Canada, Ottawa, Canada. http://www.nrc-cnrc.gc.ca/eng/solutions/advisory/egsnrc/download_egsnrc.html, 2011.
- 22 I. Kawrakow, egspc: the EGSnrc C++ class library, Technical Report PIRS-899, National Research Council Canada, Ottawa, Canada, 2005.
- 23 J. Wulff, K. Zink, and I. Kawrakow, Efficiency improvements for ion chamber calculations in high energy photon beams, *Med. Phys.* **35**, 1328–1336 (2008).
- 24 M. J. Berger, J. H. Hubbell, S. M. Seltzer, J. Chang, J. S. Coursey, R. Sukumar, D. S. Zucker, and K. Olsen, XCOM: Photon cross section database (version 1.5), Technical report, NIST, Gaithersburg, MD, <http://physics.nist.gov/xcom>, 2010.

- ²⁵ P. G. Watson and J. Seuntjens, Technical Note: Effect of explicit M and N-shell atomic transitions on a low-energy x-ray source, *Med. Phys.* **43**, 1760–1763 (2016).
- ²⁶ ICRU, Tissue Substitutes in Radiation Dosimetry and Measurements, ICRU Report 44, ICRU, Washington D.C., 1989.
- ²⁷ J. Crank, *The mathematics of diffusion*, Oxford university press, 1979.
- ²⁸ M. Chamberland, R. Taylor, D. Rogers, and R. Thomson, egs_brachy: a versatile and fast Monte Carlo code for brachytherapy, *Phys. Med. Biol.* **61**, 8214 – 8231 (2016).
- ²⁹ J. Dolan, J. V. Siebers, and J. F. Williamson, Monte Carlo and experimental dosimetry of an ^{125}I brachytherapy seed, *Med. Phys.* **33**, 4675 – 4684 (2006).
- ³⁰ NCRP Report 58, A Handbook of Radioactivity Measurements Procedures, NCRP Publications, 7910 Woodmont Avenue, Bethesda, MD. 20814 USA (1985).
- ³¹ M. K. Murphy, R. K. Piper, L. R. Greenwood, M. G. Mitch, P. J. Lamperti, S. M. Seltzer, M. J. Bales, and M. H. Phillips, Evaluation of the new cesium-131 seed for use in low-energy x-ray brachytherapy, *Med. Phys.* **31**, 1529 – 1538 (2004).
- ³² Brookhaven National Laboratory, National Nuclear Data Center, <http://www.nndc.bnl.gov/nudat2>.
- ³³ J. I. Monroe and J. F. Williamson, Monte Carlo-aided dosimetry of the Theragenics TheraSeed Model 200 ^{103}Pd interstitial brachytherapy seed, *Med. Phys.* **29**, 609 – 621 (2002).
- ³⁴ J. C. Roeske, L. Nuñez, M. Hoggarth, E. Labay, and R. R. Weichselbaum, Characterization of the theoretical radiation dose enhancement from nanoparticles, *Technology in cancer research & treatment* **6**, 395–401 (2007).
- ³⁵ J. L. Robar, S. A. Riccio, and M. Martin, Tumour dose enhancement using modified megavoltage photon beams and contrast media, *Phys. Med. Biol.* **47**, 2433 (2002).
- ³⁶ G. Cifter, J. Chin, F. Cifter, Y. Altundal, N. Sinha, E. Sajo, and W. Ngwa, Targeted radiotherapy enhancement during electronic brachytherapy of accelerated partial breast irradiation (APBI) using controlled release of gold nanoparticles, *Physica Medica* **31**, 1070–1074 (2015).
- ³⁷ R. I. Berbeco, W. Ngwa, and G. M. Makrigiorgos, Localized dose enhancement to tumor blood vessel endothelial cells via megavoltage X-rays and targeted gold nanoparticles: new potential for external beam radiotherapy, *Int. J. Radiat. Oncol. Biol. Phys.* **81**, 270–276 (2011).

- ³⁸ I. Kawrakow, Accurate condensed history Monte Carlo simulation of electron transport. I. EGSnrc, the new EGS4 version, *Med. Phys.* **27**, 485 – 498 (2000).
- ³⁹ J. Meesungnoen, J.-P. Jay-Gerin, A. Filali-Mouhim, and S. Mankhetkorn, Low-energy electron penetration range in liquid water, *Radiat. Res.* **158**, 657–660 (2002).
- ⁴⁰ H. Nikjoo, S. Uehara, D. Emfietzoglou, and F. A. Cucinotta, Track-structure codes in radiation research, *Radiat. Meas.* **41**, 1052 – 1074 (2006).
- ⁴¹ R. M. Thomson and I. Kawrakow, On the Monte Carlo simulation of electron transport in the sub-1 keV energy range, *Med. Phys.* **38**, 4531 – 4534 (2011).
- ⁴² P. Zygmanski and E. Sajo, Nanoscale radiation transport and clinical beam modeling for Gold Nanoparticle Dose Enhanced Radiotherapy (GNPT) using x-rays, *Brit. J. Radiol.*, 20150200 (2016).
- ⁴³ Y. Lin, S. J. McMahon, M. Scarpelli, H. Paganetti, and J. Schuemann, Comparing gold nano-particle enhanced radiotherapy with protons, megavoltage photons and kilovoltage photons: a Monte Carlo simulation, *Phys. Med. Biol.* **59**, 7675–7689 (2014).
- ⁴⁴ S. Jain et al., Cell-specific radiosensitization by gold nanoparticles at megavoltage radiation energies, *Int. J. Radiat. Oncol. Biol. Phys.* **79**, 531–539 (2011).
- ⁴⁵ A. McNamara, W. Kam, N. Scales, S. McMahon, J. Bennett, H. Byrne, J. Schuemann, H. Paganetti, R. Banati, and Z. Kuncic, Dose enhancement effects to the nucleus and mitochondria from gold nanoparticles in the cytosol, *Phys. Med. Biol.* **61**, 5993–6010 (2016).
- ⁴⁶ B. D. Chithrani and W. C. Chan, Elucidating the mechanism of cellular uptake and removal of protein-coated gold nanoparticles of different sizes and shapes, *Nano letters* **7**, 1542–1550 (2007).
- ⁴⁷ D. B. Chithrani, S. Jelveh, F. Jalali, M. van Prooijen, C. Allen, R. G. Bristow, R. P. Hill, and D. A. Jaffray, Gold nanoparticles as radiation sensitizers in cancer therapy, *Radiat. Res.* **173**, 719 – 728 (2010).